WALLABY Pilot Survey and ASymba: Comparing H I Detection Asymmetries to the SIMBA Simulation

Mathieu Perron-Cormier[1], Nathan Deg[1], Kristine Spekkens[1], Mark L. A. Richardson[1,2], Marcin Glowacki[3,4,5],
Kyle A. Oman[6,7], Marc A. W. Verheijen[8], Nadine A. N. Hank[8], Sarah Blyth[9], Helga Dénes[10], Jonghwan Rhee[11],
Ahmed Elagali[12], Austin Xiaofan Shen[13], Wasim Raja[13], Karen Lee-Waddell[11,13,14], Luca Cortese[11],
Barbara Catinella[11,15], and Tobias Westmeier[11]

[1] Department of Physics, Engineering Physics, and Astronomy, Queen's University, Kingston, ON, K7L 3N6, Canada; matpcormier@gmail.com
[2] Arthur B. McDonald Canadian Astroparticle Physics Research Institute, 64 Bader Lane, Kingston, ON, K7L 3N6, Canada
[3] Institute for Astronomy, University of Edinburgh, Royal Observatory, Edinburgh, EH9 3HJ, UK
[4] International Centre for Radio Astronomy Research, Curtin University, Bentley, WA 6102, Australia
[5] Inter-University Institute for Data Intensive Astronomy, Department of Astronomy, University of Cape Town, Cape Town, South Africa
[6] Institute for Computational Cosmology, Physics Department, Durham University, South Road, Durham DH1 3LE, UK
[7] Centre for Extragalactic Astronomy, Physics Department, Durham University, South Road, Durham DH1 3LE, UK
[8] Kapteyn Astronomical Institute, University of Groningen, Landleven 12, 9747 AD Groningen, the Netherlands
[9] Department of Astronomy, University of Cape Town, Private Bag X3, Rondebosch 7701, South Africa
[10] School of Physical Sciences and Nanotechnology, Yachay Tech University, Hacienda San José S/N, 100119, Urcuquí, Ecuador
[11] International Centre for Radio Astronomy Research (ICRAR), University of Western Australia, 35 Stirling Hwy, Crawley, WA 6009, Australia
[12] School of Biological Sciences, The University of Western Australia, Crawley, Western Australia, Australia
[13] CSIRO, Space and Astronomy, P.O. Box 1130, Bentley, WA 6102, Australia
[14] Australian SKA Regional Centre (AusSRC)—The University of Western Australia, 35 Stirling Highway, Crawley WA 6009, Australia
[15] Australia. ARC Centre of Excellence for All Sky Astrophysics in 3 Dimensions (ASTRO 3D), Australia
Received 2024 December 18; accepted 2024 December 27; published 2025 February 3

Abstract

An avenue for understanding cosmological galaxy formation is to compare morphometric parameters in observations and simulations of galaxy assembly. In this second paper of the ASymba: Asymmetries of H I in SIMBA Galaxies series, we measure atomic gas (H I) asymmetries in spatially resolved detections from the untargeted Widefield ASKAP L-band Legacy All-sky Blind surveY (WALLABY) survey, and compare them to realizations of WALLABY-like mock samples from the SIMBA cosmological simulations. We develop a Scanline Tracing method to create mock galaxy H I data cubes that minimizes shot noise along the spectral dimension, compared to particle-based methods, and thus minimizes spurious asymmetry contributions. We compute 1D and 3D asymmetries for spatially resolved WALLABY Pilot Survey detections, and we find that the highest 3D asymmetries ($A_{3D} \gtrsim 0.5$) stem from interacting systems or detections with strong bridges or tails. We then construct a series of WALLABY-like mock realizations drawn from the SIMBA 50 Mpc simulation volume and compare their asymmetry distributions. We find that the incidence of high A_{3D} detections is higher in WALLABY than in the SIMBA mocks, but that difference is not statistically significant (p-value = 0.05). The statistical power of quantitative comparisons of asymmetries such as the one presented here will improve as the WALLABY survey progresses and as simulation volumes and resolutions increase.

Unified Astronomy Thesaurus concepts: Galaxy structure (622); H I line emission (690); Hydrodynamical simulations (767)

1. Introduction

The gas distributions of galaxies formed in a cosmological simulation can be compared to observations in order to constrain the galaxy formation model and determine the underlying drivers of galaxy morphology. These comparisons allow explorations of how this morphology is influenced by cosmological parameters, local environment effects, subgrid physics, and more.

Effective comparisons between observations and simulations require robust methods of creating mock observations from the simulated particle distributions. In atomic gas (H I), the Mock Array Radio Telescope Interferometry of the Neutral ISM (MARTINI) code (K. A. Oman 2019, 2024; K. A. Oman et al. 2019) is widely used. Designed for high-resolution smoothed

particle hydrodynamics (SPH) simulations, it has been widely used to compare the properties of well-resolved H I observations and simulated H I distributions (e.g., P. V. Bilimogga et al. 2022; M. Glowacki et al. 2022). At low particle numbers, however, the effects of shot noise begin to become apparent in the mocks, notably along the spectral axis.

Also required for comparisons between simulations and observations is a method to quantify galaxy morphology. One approach is the Concentration–Asymmetry–Clumpiness "CAS" (C. J. Conselice 2003) set of parameters. These parameters have been shown to be reliable for relatively high-resolution H I observations (B. W. Holwerda et al. 2011; N. Giese et al. 2016; P. V. Bilimogga et al. 2022). Notably, spatial H I asymmetries in galaxies are connected to interactions (B. W. Holwerda et al. 2011), accretion events (R. Sancisi et al. 2008), and starbursts (F. Lelli et al. 2014) for various samples of gas-rich galaxies. On the simulation side, J. Gensior et al. (2024) found that H I spatial asymmetry is a promising observable to compare different simulation models with observations.

Despite their utility at high resolution, both H I and optical spatial asymmetries wane at low angular resolutions, and noise introduces important systematic effects (N. Giese et al. 2016; M. D. Thorp et al. 2021). For example, using mock galaxies in H I from the EAGLE simulation, P. V. Bilimogga et al. (2022) found that both spatial and spectral asymmetries are robust only at high resolution and signal-to-noise ratio (S/N). In particular, the resolution requirements for robust spatial asymmetries strongly limit their application to H I maps of galaxies from untargeted surveys such as the Widefield Australian Square Kilometre Array Pathfinder (ASKAP) *L*-band Legacy All-sky Blind surveY (WALLABY; B. S. Koribalski et al. 2020; N. Deg et al. 2022; T. Westmeier et al. 2022), which will image an unprecedented number of detections—most of which will, however, be only marginally spatially resolved.

By contrast, spectral asymmetries such as lopsidedness (M. P. Haynes et al. 1998; D. Espada et al. 2011; J. Bok et al. 2019; A. B. Watts et al. 2023) and channel-by-channel profile asymmetries (N. Deg et al. 2020; T. N. Reynolds et al. 2020) are useful for characterizing asymmetries with low spatial resolution but high spectral resolution that are characteristic of deep H I surveys such as Deep Investigation of Neutral Gas Origins (J. Rhee et al. 2023) and Looking At the Distant Universe with the MeerKAT Array (S. Blyth et al. 2016).

To explore asymmetries as a tool for upcoming H I surveys, M. Glowacki et al. (2022) introduce ASymba: Asymmetries of H I in SIMBA Galaxies, which uses the SIMBA cosmological simulation suite (R. Davé et al. 2019) to connect measured asymmetries to the physical drivers of galaxy evolution. M. Glowacki et al. (2022) find that spectral asymmetries of SIMBA mock cubes correlate strongly with H I mass, as well as with the number of mergers that a galaxy has undergone. However, the high-resolution merging galaxy simulations by N. Deg et al. (2020) show that spectral asymmetries depend on observing parameters such as galaxy sky orientation and inclination, muddling their connection to the underlying galaxy structure. Using an alternative spectral H I asymmetry metric, A. B. Watts et al. (2020) compared galaxies from the TNG simulation (D. Nelson et al. 2019) to show that, while in many cases there is a connection with environment (satellites are more asymmetric than centrals as a population, as seen in observations; e.g., A. B. Watts et al. 2020), central galaxies can also be asymmetric.

In light of the shortcomings of spatial and spectral asymmetries applied to H I surveys, N. Deg et al. (2023) developed a 3D asymmetry measure that leverages the full dimensionality of the H I data cubes, outperforming spatial and spectral asymmetries for marginally spatially resolved detections in surveys such as WALLABY. N. Deg et al. (2023) also apply a squared differences background correction approach that provides a significant improvement to the calculation of asymmetries in the low-S/N regime compared to more conventional absolute differences (see also E. Sazonova et al. 2024 and S. Wilkinson et al. 2024).

While there are many works that examine morphometrics in simulations (e.g., J. M. Lotz et al. 2008, 2010; M. W. Abruzzo et al. 2018; M. D. Thorp et al. 2021; P. V. Bilimogga et al. 2022; M. Glowacki et al. 2022; S. Wilkinson et al. 2024) and in observations (e.g., C. J. Conselice 2003; B. W. Holwerda et al. 2011, 2023; N. Giese et al. 2016; J. Bok et al. 2019; T. N. Reynolds et al. 2020), relatively few have directly compared asymmetries between them (e.g., K. M. Hambleton et al. 2011;

N. Deg et al. 2020). With WALLABY pilot survey observations, a promising new 3D asymmetry technique, and an initial exploration of asymmetries in SIMBA now in hand, we proceed to develop a new method to create mock data cubes and compare measured WALLABY asymmetries to simulated SIMBA ones for the first time.

In this second paper of the ASymba series, we perform a quantitative comparison between 1D and 3D H I asymmetries measured for spatially resolved WALLABY Pilot Survey detections and WALLABY-like mock cubes derived for simulated SIMBA galaxies.

Section 2 describes the WALLABY and SIMBA datasets that we analyze. Section 3 describes our process for generating mock cubes using a Scanline Tracing approach, and its impact on asymmetries measured from noiseless WALLABY-like cubelets. Section 4 presents our mock WALLABY sample from SIMBA and compares it to the WALLABY sample. Finally, Section 5 discusses our results.

2. Datasets

2.1. WALLABY

WALLABY is an untargeted H I survey on the ASKAP (A. W. Hotan et al. 2021) covering about 14,000 square degrees of the southern sky. It has a spatial resolution of $30''$, a spectral resolution of 18.5 kHz (which corresponds to $\sim 4\,\mathrm{km\,s}^{-1}$ at $z \sim 0$), and a target sensitivity of 1.6 mJy beam^{-1}, allowing it to detect the H I content of $\sim 2 \times 10^5$ galaxies (T. Westmeier et al. 2022; C. Murugeshan et al. 2024). Simulated predictions from B. S. Koribalski et al. (2020), adjusted for the survey area in T. Westmeier et al. (2022) and C. Murugeshan et al. (2024), suggest that ~ 2300 galaxies will be spatially resolved by more than 5 beams, with $> 10^4$ being marginally resolved.

WALLABY Pilot observations of a number of fields have been released in T. Westmeier et al. (2022) and C. Murugeshan et al. (2024), consisting of ~ 2400 detections and 236 kinematic models. A WALLABY detection may consist of more than a single galaxy due to limitations in the resolution, S/N, and source finding. At only 1% of the total WALLABY volume, the pilot observations already comprise the largest sample of uniformly analyzed interferometric observations of the H I content in galaxies. This is an ideal sample for studying with morphometrics (B. W. Holwerda et al. 2023), which is why we have chosen it as our testbed for comparing simulated asymmetries with observations.

2.2. SIMBA

SIMBA (R. Davé et al. 2019) is a cosmological simulation that runs on the GIZMO hydrodynamical solver (P. F. Hopkins 2015) in Meshless Finite Mass (MFM) mode. The simulation uses the GRACKLE library (B. D. Smith et al. 2016) to implement radiative cooling and photoionization heating. The H I fraction of the gas is evolved with the simulation instead of computed in post-processing, following the method of R. Davé et al. (2017). We have chosen to utilize the 50 Mpc box for this work, which contains 512^3 particles in a comoving $(50\ h^{-1}\ \mathrm{Mpc})^3$ volume with a gas particle mass resolution of $1.82 \times 10^7\,M_\odot$. In this box, the minimum full width at half maximum (FWHM) smoothing length of the particles is ~ 0.7 kpc.

The choice of the 50 Mpc box is motivated by the need for a large number of well-resolved H I galaxies in the mass range of the WALLABY detections (see Section 4.1). The other

iterations of the 50 Mpc simulation with different feedback methods (for example,with no active galactic nucleus), would also allow future studies of how those physics drive changes in morphology.

Galaxies are identified using the CAESAR catalog. To avoid effects from poor numerical resolution, we follow the selection criteria of M. Glowacki et al. (2020) to select systems for this study, namely

1. $M_{\mathrm{H\,I}} > 10^9\,M_\odot$,
2. $M_\star > 5.8 \times 10^8\,M_\odot$,
3. sSFR $> 1 \times 10^{-11}\,\mathrm{yr}^{-1}$,

and to ensure that only galaxies that are numerically well resolved are selected, we impose

4. $N_{2\,\mathrm{kpc}} > 100$,

where $N_{2\,\mathrm{kpc}}$ is the number of fluid elements with smoothing length FWHM below 2 kpc. Out of 5218 SIMBA galaxies, 789 fall within these criteria.

3. SIMBA Mock Cubes

To compare WALLABY detections to SIMBA systems, it is necessary to generate mock observations of the latter that have noise and resolution similar to those of the WALLABY data cubes.

However, we show in Section 3.1.1 that widely used methods of generating mock H I cubes tend to produce significant artificial shot noise contributions to noiseless WALLABY-like mocks. As a result, we present a new Scanline Tracing method for generating mock cubes from simulations in Section 3.1.2. Section 3.2 illustrates the impact of adopting this new method on the asymmetry measures defined by N. Deg et al. (2023) for a suite of noiseless mock SIMBA detections.

3.1. Mock Observations

Cosmological simulations evolve sets of discrete elements that represent continuous fluids such as gas. The SPH (see R. A. Gingold & J. J. Monaghan 1977; L. B. Lucy 1977) and MFM techniques of interest for this paper are two methods of discretizing the fluid equations. In our case, a mock H I observation consists of the transformation of the numerical elements of a simulation into an H I cube measured as $f_{i,j,k}$, where the i, j, k indices denote spatial and spectral indices allowing the voxel of the data cube to be specified. While the cube is measured in discrete coordinates, it will be easier in the following derivations to write its coordinates in terms of continuous sky variables $f(x, y; v)$.

To model gases, such as H I, SPH methods use a kernel W to interpolate a given field ϕ between particles:

$$\phi_s(\boldsymbol{x}) = \sum_n \phi_n V_n W(\boldsymbol{x}-\boldsymbol{x}_n;\, h_n), \qquad (1)$$

with ϕ_s being the smoothed field, $\boldsymbol{x}$ the position, V the volume, and h the smoothing length. Here, the n indices iterate over the particles and their properties. At sufficient resolution, $\phi_s \approx \phi$. The MFM technique introduces a local normalization to the total kernel; the nth particle's MFM kernel ψ_i relates to the

SPH kernel W according to the definition

$$\psi_n(\boldsymbol{x}) \equiv \frac{W(\boldsymbol{x}-\boldsymbol{x}_n;\, h_n)}{\sum_m W(\boldsymbol{x}-\boldsymbol{x}_m;\, h_m)}, \qquad (2)$$

where m iterates over all particles. MFM smoothed fields are calculated akin to SPH:

$$\phi_s(\boldsymbol{x}) = \sum_n \phi_n \psi_n(\boldsymbol{x}). \qquad (3)$$

3.1.1. Particle-built Mock Cubes

MARTINI (K. A. Oman 2019, 2024; K. A. Oman et al. 2019) is a widely used method for generating mock H I data cubes. By default, MARTINI extends Equation (1) to an assumed particle Gaussian distribution along the frequency axis; this distribution is evaluated individually and then added to produce the particle method's intensity f_p at a given spatial and spectral coordinate:

$$f_p(x, y;\, v) \equiv \sum_n s_n(v-v_n;\, \sigma_n) V_n \int_{\mathbb{R}} W(\boldsymbol{x}-\boldsymbol{x}_n;\, h_n)\, dz, \qquad (4)$$

with σ_n denoting the broadening corresponding to the particle temperature, s_n representing a Gaussian spectrum corresponding to the particle, and z being the line-of-sight axis.

While this method has been used to study asymmetries in both the EAGLE simulation (P. V. Bilimogga et al. 2022), and the SIMBA simulation (M. Glowacki et al. 2022), the approximations in Equation (4) can cause issues. To illustrate, we have selected two representative SIMBA sources, Galaxy 467 and Galaxy 1531, and generated noiseless mock observations of them using MARTINI. Moment 0 (intensity) and Moment 1 (velocity) maps and spectra for the two MARTINI realizations are shown in the left-hand columns of Figures 1 and 2, while the upper panels of Figures 3 and 4 show 3D renderings of the MARTINI cubes generated through the use of SLICERASTRO (D. Punzo et al. 2017).

Galaxy 467 has a relatively high particle number (~1600), but the spectrum in the lower left panel of Figure 1 is fairly jagged. We attribute this to shot noise caused by the superposition of Gaussians. While SPH and MFM elements tend to be spatially distributed in a meaningful way, this is not necessarily the case in velocity space. Certain parts of the velocity field may be over- or undersampled, leading to the observed jagged features. This noise is more significant at the lower particle number in Galaxy 1531 (lower left panel of Figure 2). The jaggedness of these spectra will artificially increase both 1D and 3D asymmetries. This issue is not present in the P. V. Bilimogga et al. (2022) study of EAGLE asymmetries, due to both the higher particle resolution of EAGLE as well as their application of Hanning smoothing to their spectra.

The spectral jaggedness of these MARTINI cubes can be understood by examining the behavior of a pair of particles separated in velocity space. Applying Equation (4) to these particles leads to distinct peaks when the particle velocities are sufficiently separated relative to their temperature, regardless of their smoothing lengths. If the velocity, density, and temperature fields were instead evaluated separately according to either, for SPH, Equation (1) or, for MFM, Equation (3), the spectrum would be washed out of spectral features for
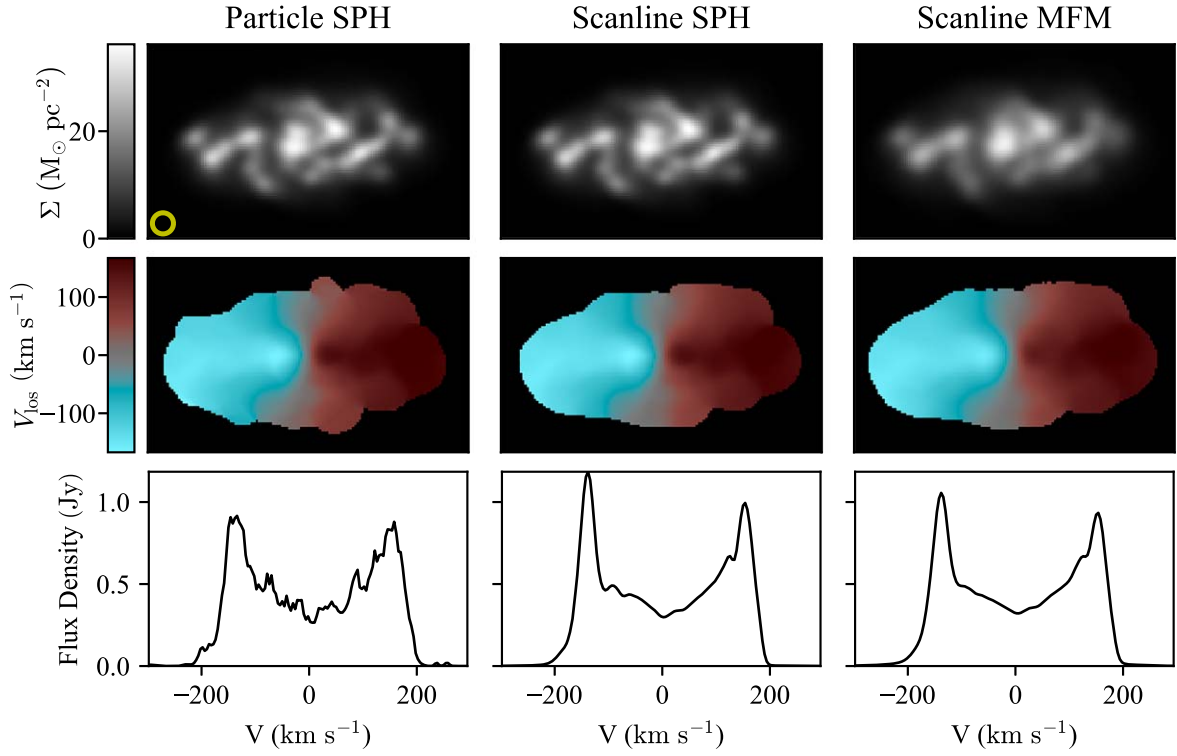
Figure 1. Moment 0 maps (top), moment 1 maps (middle), and spectra (bottom) for the Particle SPH (left), Scanline Tracing SPH (middle), and MFM (right) constructed from noiseless mock H I cubes of Galaxy 467 of the SIMBA 50 Mpc simulation taken at a distance of 20 Mpc with WALLABY observation parameters. The ring in the bottom left corner of the first moment 0 map shows the beam FWHM. For the moment 1 maps, the cube is masked at a threshold of 1.6 mJy beam^{-1} (approximately the WALLABY noise rms) and we use the CosmosCanvas (J. English et al. 2024) color map. The galaxy is composed of ~1600 collisional particles and has an H I mass of ~$1.8 \times 10^{10} M_{\odot}$.
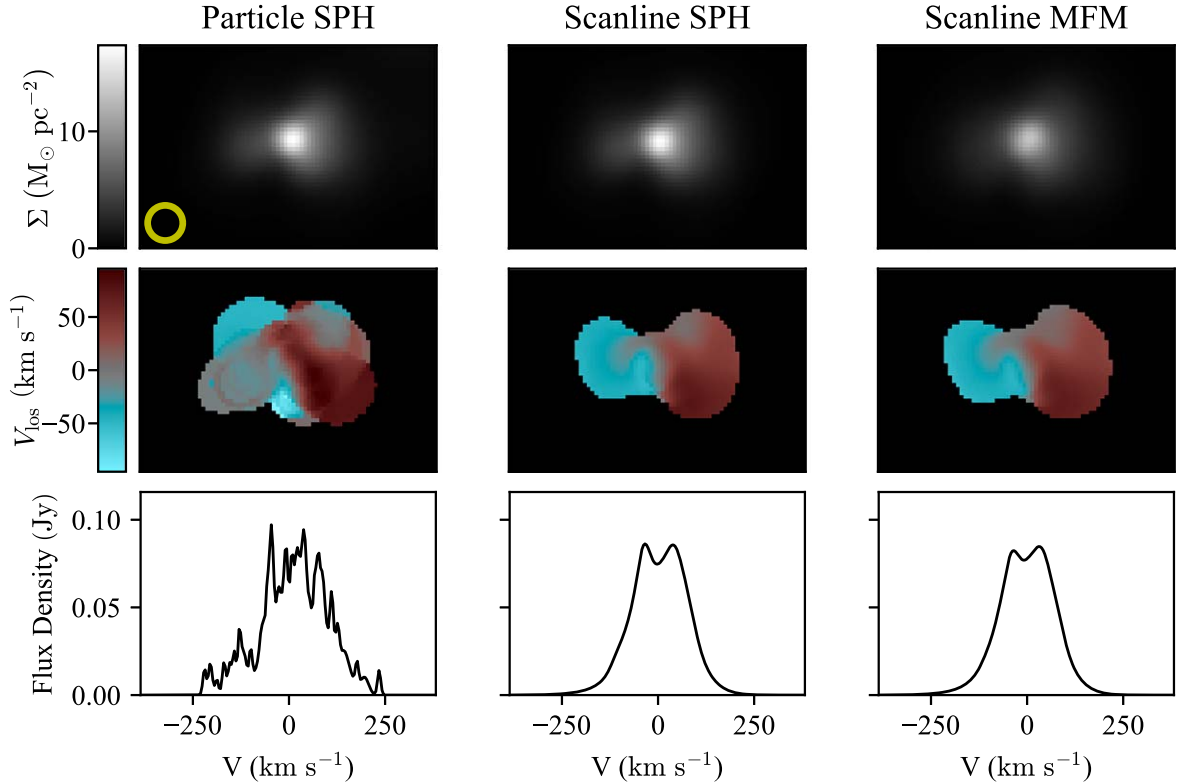
Figure 2. Same as Figure 1, but for a noiseless, WALLABY-like mock of Galaxy 1531. The galaxy is composed of ~1100 collisional particles and has an H I mass of ~$1.5 \times 10^{9} M_{\odot}$.

Galaxy 467

Particle SPH

$A_{3D} = \quad 0.55$

Scanline SPH

$A_{3D} = \quad 0.56$

Scanline MFM

$A_{3D} = \quad 0.49$
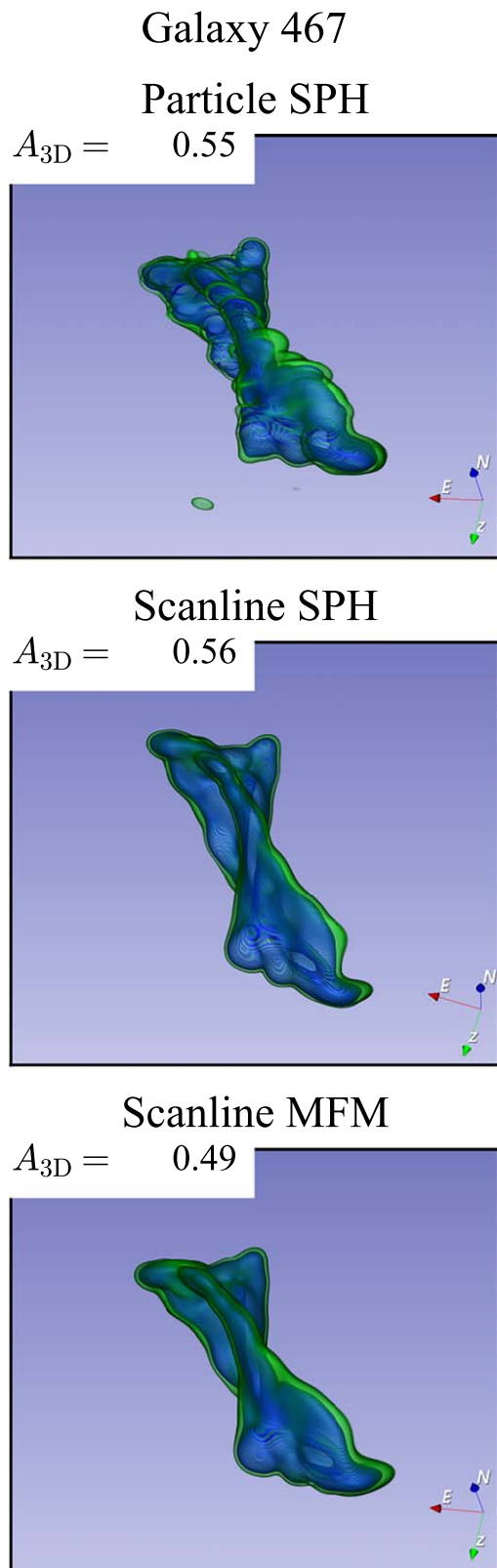
Figure 3. SLICERASTRO view of noiseless mocks of the H I cube of Galaxy 467 presented in Figure 1 for the particle SPH (top), scanline SPH (middle), and scanline MFM (bottom). The *E–N–Z* axes show the R.A.–decl.–velocity axes, respectively, with +*Z* indicating the approaching velocity. The values of A_{3D} for each mock, computed around the minimum of the potential, are given in the top left corner of each panel.

Galaxy 1531

Particle SPH

$A_{3D} = \quad 0.65$

Scanline SPH

$A_{3D} = \quad 0.36$

Scanline MFM

$A_{3D} = \quad 0.33$
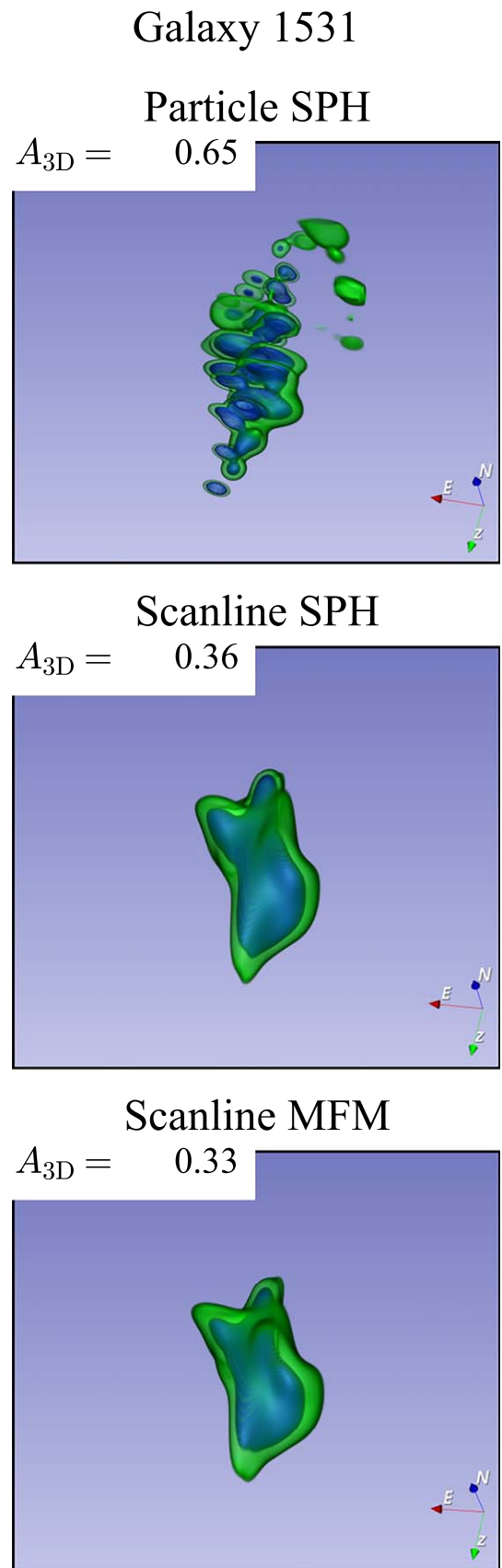
Figure 4. Same as in Figure 3, but for Galaxy 153 presented in Figure 2.

sufficiently large smoothing lengths, regardless of the particle temperatures and velocities. This is a consequence of the SPH and MFM interpolation schemes not being invariant under transformation. For example, if a field ϕ were interpolated and then squared, it would yield a different field than if its square were directly interpolated:

$$\left(\sum \phi_n V_n W(\boldsymbol{x}-\boldsymbol{x}_n; h_n)\right)^2 \neq \sum \phi_n^2 V_n W(\boldsymbol{x}-\boldsymbol{x}_n; h_n).$$

Effectively, Equation (4) introduces shot noise instead of the expected oversmoothing from SPH at low resolutions. According to Equation (1), there should be intermediate regions of the gas where the maximal spectral intensity corresponds to mediating velocities. However, this behavior is not enforced by Equation (4) unless the particles sample these regions of the velocity field. Additionally, Equation (4) is unlikely to create a spectrum that is locally Gaussian, whereas Equation (1) enforces this. The appearance of the different points in the spectrum can be attributed to the spectral separation of the particles being lower than their dispersion σ_n^2. While the particle-based spectra can be smoothed by artificially injecting additional velocity dispersion into each particle, this is unphysical. Instead, we develop a different method of computing mock H I data cubes that directly sample the fields.

3.1.2. Scanline Tracing

The MARTINI realizations of Galaxies 467 and 1531 shown in Figures 1–4 and discussed in Section 3.1.1 suggest that, for our specific asymmetry analysis of SIMBA galaxies, a new method of generating mock H I cubes is needed. To that end, we adopt a *scanline* method, where the underlying fields are sampled via scanlines cast through simulation space along "observed" lines of sight. For our purposes, the small angle approximation holds and the scanlines are held parallel. To simplify the math, we will hold the line of sight as being in the z-axis. The scanlines sample the fields at set intervals, resulting in a 3D grid of the simulation space that can then be collapsed into a data cube.

The spectrum is calculated as a function of the fields for a given position:

$$s(\boldsymbol{x}, v) \equiv \frac{\rho(\boldsymbol{x})}{\sqrt{2\pi\sigma^2(\boldsymbol{x})}} \exp\left(-\frac{(v - v_z(\boldsymbol{x}))^2}{2\sigma^2(\boldsymbol{x})}\right), \qquad (5)$$

with $\rho(\boldsymbol{x})$, $v_z(\boldsymbol{x})$, and $\sigma(\boldsymbol{x})$ being the H I density, line-of-sight velocity, and thermal velocity dispersion fields of the fluid at a given position $\boldsymbol{x}$, and v being the velocity at which the spectrum's intensity is measured. In the case of MFM, the velocity is treated such that the quantity of movement of a fluid element is defined as equal to that of the integral of the quantity of movement of the fluid over the particle's effective volume, but we consider the interpolation of the velocity field to also be reasonable.

The spectra encountered by the scanlines at each step dz along the line of sight are collapsed into the spectrum at a given coordinate x, y on the sky. For a pixel of width Δx and height Δy, this gives

$$f(x, y; v) = \int_{x-\frac{\Delta x}{2}}^{x+\frac{\Delta x}{2}} \int_{y-\frac{\Delta y}{2}}^{y+\frac{\Delta y}{2}} \int_{\mathbb{R}} s(\boldsymbol{x}', v)dx'dy'dz'.$$

To approximate this integral, we evaluate the local smoothed spectrum $s_s(\boldsymbol{x}, v)$ at set intervals with sampled $\rho_s(\boldsymbol{x})$, $\sigma_s^2(\boldsymbol{x})$, $v_s(\boldsymbol{x})$ fields using Equation (1) or (3) as appropriate.

The density can be measured according to the SPH formalism:

$$\rho_s(\boldsymbol{x}) = \sum_n m_n W(\boldsymbol{x} - \boldsymbol{x}_n; h_n), \qquad (6)$$

with m_n being the mass of the nth particle. Since only the H I mass is of interest to us, we calculate the densities using the particle H I masses instead of their total masses. This equation ensures that the mass is conserved for a kernel W normalized under integration. This version of the density calculation agrees with the particle-based densities.

In MFM, the conserved quantities are considered as averaged over the particle volume. The particle density cannot be measured directly because the kernel is not normalized under integration. The particle effective volume is defined as

$$V_n \equiv \iiint_{\mathbb{R}^3} \psi_n(\boldsymbol{x})d^3\boldsymbol{x},$$

such that the particle density is $\rho_n = m_n/V_n$. However, this would require the evaluation of the integral of the kernel, which is nonelementary. For particles fully contained by the Scanline Tracing box of domain $\mathbb{B}$, the volume can be estimated by summation. For particles that are not contained by the box, the volume is scaled up according to the volume across which the particle's kernel is nonzero. The volume is then evaluated:

$$V_n \approx \begin{cases} \sum_{\psi_n \neq 0} \psi_n \Delta V & \text{if } \boldsymbol{x}_n + \boldsymbol{h}_n \in \mathbb{B} \ \forall \ \boldsymbol{h}_n \\ \dfrac{\iiint_{W(\boldsymbol{x};h_n)\neq 0} d^3\boldsymbol{x} \sum_{\psi_n \neq 0} \psi_n \Delta V}{\sum_{\psi_n \neq 0} \Delta V}, \end{cases} \qquad (7)$$

where ΔV is the volume element of the 3D grid across which the fields are evaluated, and $\boldsymbol{h}_n$ is an arbitrary vector of length h_n. The integral corresponds to the volume where the kernel is nonzero. Using for example a kernel where $W(\boldsymbol{x} - \boldsymbol{x}_n; h_n) = 0 \ \forall \ |\boldsymbol{x} - \boldsymbol{x}_n| > h_n$, the integral gives the sphere $4\pi h_n^3/3$. With the volume, the density can be calculated locally with

$$\rho_s(\boldsymbol{x}) = \sum_n \frac{m_n}{V_n} \psi_n(x). \qquad (8)$$

When particles fall completely inside the sampled box, Equation (7) ensures that Equation (8) will always give a density contribution consistent with the particle total mass if the density is evaluated at the same points as those used to evaluate the volume. The other fields are interpolated using Equation (3).

The SIMBA simulation uses the cubic spline kernel:

$$W(\boldsymbol{x}; h) = \frac{1}{h^3} w\left(\frac{|\boldsymbol{x}|}{h}\right), \qquad (9a)$$

$$w(q) \equiv \frac{8}{\pi} \begin{cases} 1 - 6q^2(1-q) & \text{if } q \leqslant 1/2 \\ 2(1-q^3)^3 & \text{if } 1/2 < q \leqslant 1 \\ 0 \end{cases}$$

(9b)

Once the fields are obtained, Equation (5) is evaluated at each spectral channel Δv. The sampled spectra are then added to approximate the integral along the scanline:

$$f(x, y; v)$$
$$\approx \Delta V \sum_{i=-\frac{N_{\text{line}}}{2}}^{\frac{N_{\text{line}}}{2}} \frac{\rho_s(x, y, i\Delta z)}{\sqrt{2\pi\sigma_s^2(x, y, i\Delta z)}} e^{-\frac{(v-v_s(x,y,i\Delta z))^2}{2\sigma_s^2(x,y,i\Delta z)}},$$ (10)

with N_{line} being the number of times each scanline samples the fluid fields. This allows each pixel to have spectral structure, but enforces that the spectrum of the gas is locally Gaussian. Finally, the pixels are assembled from the rays and are convolved according to a desired beam to create a data cube. The pixels are often oversampled to ensure that their size does not alter the spectrum.

For our specific case, we construct cubes at resolutions of half the minimum smoothing length. After being calculated at this resolution, cubes are downsampled to the desired resolution using the OPEN CV2 pixel-area relation INTER_ AREA (G. Bradski 2000). The cube is constructed for a region encompassing all the gas that can contribute to a moment 0 map above the noise level at a 10 Mpc distance extended by two beams at the specified observation distance. Relaxing these parameters does not meaningfully alter the results of Sections 3.2 and 4.

With this formalism, it is possible to construct mock cubes using Scanline Tracing for either SPH or MFM. The middle columns of Figures 1 and 2 show the moment maps and spectra for noiseless Scanline SPH realizations of Galaxies 467 and 1531 from SIMBA, while the right-hand column shows the Scanline MFM realization. Similarly, the middle and lower panels of Figures 3 and 4 show the 3D renderings of the SPH and MFM realizations. The Scanline Tracing mocks for both Galaxy 467 and 1531 show little evidence of shot noise. For Galaxy 1531, the Scanline mocks have a narrow, double-peaked profile. Moreover, in this lower-particle-number, lower-mass regime, the Scanline Tracing method dramatically changes the moment 1 maps. This demonstrates that the Scanline tracing causes this change, rather than the assumption of using SPH or MFM to construct the cubes.

The comparison of the Scanline MFM realizations to the Scanline SPH realizations has a much smaller effect on the mock cube. The spectra are slightly smoother and the moment 0 maps appear to be slightly less well resolved. This is due to the MFM kernel normalization distributing more gas to regions where there is less particle overlap.

3.2. SIMBA Asymmetries

To fully understand the differences between Particle-generated cubes and Scanline Tracing–generated cubes for measuring asymmetries, we made mock observations of the 789 SIMBA galaxies that satisfy our criterion in Section 2.2 using both the particle-based MARTINI and our new Scanline Tracing MFM method. The mock cubes have a resolution of

$30''$ and 4 km s^{-1}, matching WALLABY, though they are noiseless in order to better probe the impact of the different approaches. For this test, all galaxies are placed at a distance of 20 Mpc (where $1 \text{ kpc} = 10''$ on the sky), with an inclination of $60°$ (calculated based on the angular momentum vector). This distance allows for sufficient resolution elements for calculating the spatial asymmetry.

With the two suites of noiseless SIMBA cubes generated, we calculate their spectral (1D), spatial (2D), and 3D asymmetry using the 3D Asymmetries in data CubeS (3DACS; N. Deg et al. 2023) code. The asymmetry formula in the idealized noiseless case is

$$A^2 = \frac{P}{Q},$$ (11)

where P and Q are the squared odd and even parts of the chosen distribution, respectively:

$$P = \sum_i (f_i - f_{\bar{i}})^2,$$ (12a)

$$Q = \sum_i (f_i + f_{\bar{i}})^2.$$ (12b)

The bold $\boldsymbol{i}$ indices denote that we can compute the asymmetry over any number of dimensions, collapsing the others before-hand, then computing the asymmetry using Equations (12) and (11):

$$f_{\boldsymbol{i}=(k)} = \sum_{i,j} f_{i,j,k} \quad \text{for} \quad A_{1D},$$ (13a)

$$f_{\boldsymbol{i}=(i,j)} = \sum_k f_{i,j,k} \quad \text{for} \quad A_{2D},$$ (13b)

$$f_{\boldsymbol{i}=(i,j,k)} \quad \text{for} \quad A_{3D}.$$ (13c)

We note that A_{1D} as defined above is equivalent to the channel-by-channel asymmetry developed by N. Deg et al. (2020) and T. N. Reynolds et al. (2020).

A critical component of the asymmetry is the center point about which the pairs of fluxes are compared. Both the MARTINI Particle mocks and our Scanline Tracing mocks are centered at the minimum of total potential spatially and the bulk velocity of the particles. This center is computed according to the particle data, making it independent of the chosen mock method (SPH-Particle or MFM/SPH Scanline Tracing). The H I gas is not always centered at this potential minimum, which can cause large asymmetries.

Before proceeding to the full distribution of asymmetries, it is worth returning to our two example galaxies. The upper left corner of each panel in Figures 3 and 4 provides the 3D asymmetry for the MARTINI Particle SPH, Scanline SPH, and Scanline MFM realizations of Galaxies 467 and 1531, respectively. Given that $0 \leqslant A_{3D} \leqslant 1$ in the noiseless case (see Section 4 for a discussion of the effect of noise), the differences between the Particle and Scanline MFM realizations are significant. This is particularly true in the low particle number regime of Galaxy 1531.

This difference holds for the majority of SIMBA galaxies. Figure 5 shows the difference between the Particle SPH 3D asymmetries and Scanline MFM 3D as a function of H I mass. The Particle SPH asymmetries are usually larger than their Scanline MFM counterparts. Particle SPH realizations are more asymmetric by as much as $\Delta A_{3D} \sim 0.3$, mostly due to shot
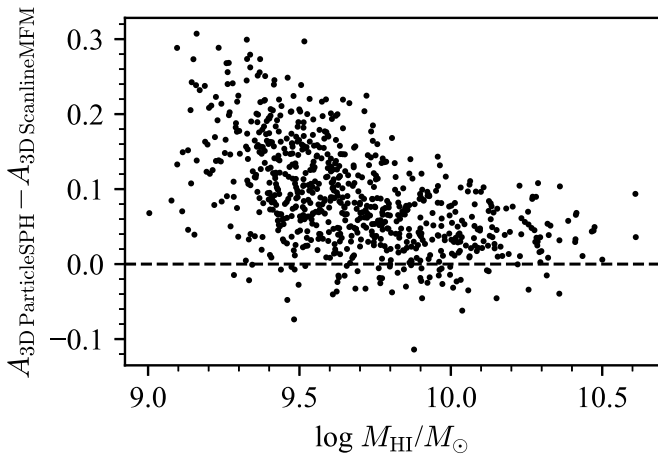
Figure 5. Plot of the difference of 3D asymmetry between the Particle SPH and MFM Scanline Tracing realizations of SIMBA mock cubes described in Section 2.2 as a function of the cube H I mass.

Figure 6. Comparison of 1D and 2D asymmetries of noiseless, WALLABY-like, Scanline MFM mocks of SIMBA galaxies. The dashed black line shows the 1:1 relation. The points are colored by H I mass, which correlates to resolution by virtue of the size–mass relation (J. Wang et al. 2016).

Figure 7. Same as in Figure 6, except for the combination of 1D and 2D asymmetries plotted against 3D asymmetry. Ten H I sources fall outside the 0, 1 range for the combined $A_{1D} + A_{2D}$.

noise. However, the differences decrease with increasing mass and therefore increasing particle number. As such, at higher particle resolutions, the MARTINI Particle SPH realizations will likely converge to the Scanline MFM realizations, making the specific method of generating mock observations less critical. Since we wish to compare SIMBA galaxies with as few as 1000 particles to WALLABY detections, we exclusively use the Scanline Tracing MFM method of generating mock SIMBA cubes hereafter.

Before turning to WALLABY comparisons in Section 4, it is worth exploring the relationship between 1D, 2D, and 3D asymmetries for noiseless Scanline MFM mocks. N. Deg et al. (2023) examined these measures using idealized mock cubes generated through a modified version of the Mock Cube Generator Suite (MCGSUITE; N. Deg & K. Spekkens 2019) code where asymmetries were introduced as first Fourier moments. This type of asymmetry—lopsidedness—is discussed in H.-W. Rix & D. Zaritsky (1995) and D. Zaritsky & H.-W. Rix (1997). N. Deg et al. (2023) found that A_{1D}, A_{2D}, and A_{3D} increase linearly with lopsidedness, and thus that all asymmetries in their analysis are correlated. Here, we use SIMBA to explore whether or not these correlations persist for asymmetries produced by simulated cosmological galaxy assembly.

In Figure 6, we plot the recovered 1D and 2D asymmetries for the Scanline Tracing MFM cubes, colored by their H I mass. We find that spectral (1D) and spatial (2D) asymmetries are not strongly correlated, supporting the findings of P. V. Bilimogga et al. (2022). It is possible that the drivers of spectral and spatial asymmetries are different, which would lead to uncorrelated asymmetries. However, the measured asymmetry also depends on the adopted center point, and the H I gas in SIMBA galaxies is not always centered at the minimum of the potential. Second, asymmetry tends to be correlated with resolution, in particular in the low-resolution regime (N. Giese et al. 2016; N. Deg et al. 2023). The spatial and spectral resolutions are effectively independent. At low spatial resolutions, the spatial asymmetry will go to zero, leaving the spectral asymmetry intact, which again will hide any possible correlations. N. Deg et al. (2023) argue that robust measures of the 2D asymmetry require ~7 or more resolution elements (see also N. Giese et al. 2016;
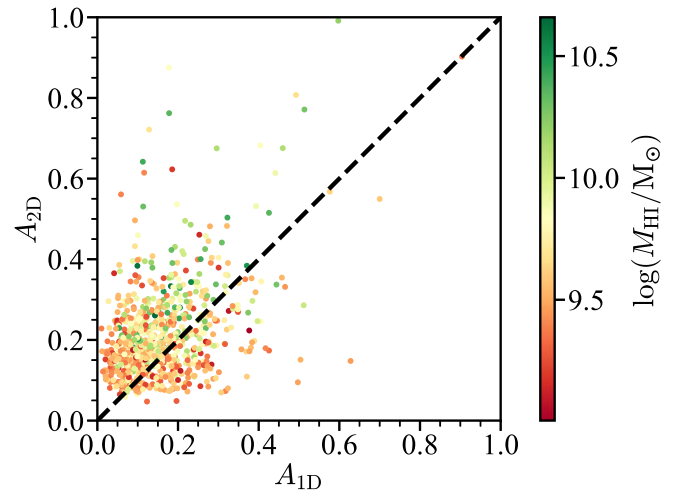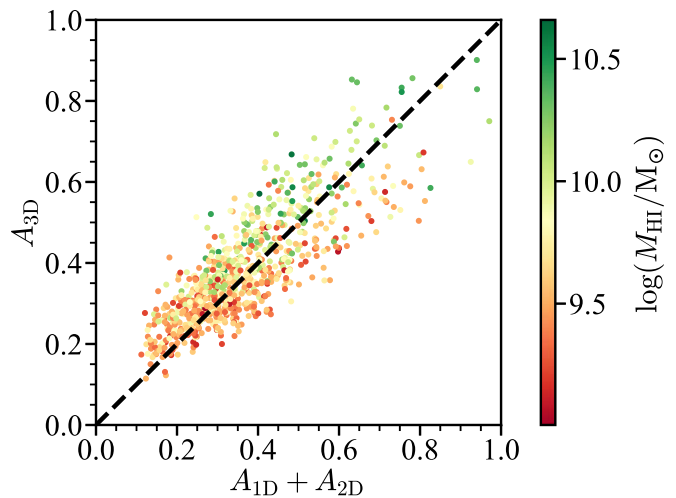
M. D. Thorp et al. 2021). This requirement is satisfied for this particular sample of mock SIMBA galaxies at 20 Mpc with a 30″ beam, but it is not true for the majority of the WALLABY observations (see Section 4).

The A_{3D} measure was designed to capture both spectral and spatial asymmetries in H I data cubes (N. Deg et al. 2023). This is illustrated in Figure 7, which shows a comparison of A_{3D} to $A_{1D} + A_{2D}$. To focus on the most important range, we have cut the full dynamical range of $A_{1D} + A_{2D}$, which extends to 2, and 10 H I mocks with $A_{1D} + A_{2D} > 1$ are missing. Comparing the A_{3D} in this figure to either the 1D or 2D asymmetry distributions in Figure 6 shows that the 3D asymmetries span a larger dynamic range than either 1D or 2D for the noiseless WALLABY-like SIMBA mocks. We note that, in Figure 6, the high- and low-mass mock cubes split along the 1:1 line, with the high-mass cubes trending to higher A_{3D} for a given $A_{1D} + A_{2D}$ whereas the low-mass mocks fall below this line. This bifurcation can be explained by resolution effects

impacting the spatial (2D) component of the asymmetry, as, at fixed distances, H I mass is correlated to resolution through the H I size–mass relation (J. Wang et al. 2016). Figures 6 and 7 demonstrate that the advantages of A_{3D} over A_{1D} and A_{2D} posited by N. Deg et al. (2023) using idealized mocks are also evident in more complicated cosmologically generated mocks.

4. Asymmetries and the Mock WALLABY Sample

We now quantitatively compare the asymmetries in WALLABY Pilot Survey detections to those found in SIMBA. Section 4.1 describes the asymmetries of the WALLABY detections, and Section 4.2 contains the comparison of the two.

4.1. WALLABY Asymmetries

One key difference between WALLABY Pilot Survey detections and the mock observations examined in Section 3.2 is noise. Noise tends to increase the asymmetry, but N. Deg et al. (2023) developed a correction to the squared difference asymmetry used here:

$$A = \left(\frac{P - B}{Q - B} \right)^{1/2}, \qquad (14)$$

where P and Q are the numerator and denominator of Equation (11), respectively, as given by Equation (12), and B is the background correction. Assuming Gaussian noise, $B = 2N\sigma^2$, where N is the number of voxels/pixels/channels used in the asymmetry calculation and σ is the rms noise level (N. Deg et al. 2023). This correction can still fail for very low-S/N detections. In some cases, the signal and noise can be such that $P < B$. When $P < B$, we set $A = -1$ as an indication that there is no measured intrinsic asymmetry, but rather that the full signal from P/Q in Equation (11) can be attributed to the noise. This correction is more likely to fail for A_{3D} than for A_{1D}, because the signal is integrated before computing the spectral asymmetry.

Second, in real observations, the minimum of the potential is unknown, so a different center must be used in the asymmetry calculation relative to that adopted in Section 3.2. For simplicity, we use the center found by the WALLABY source finding. WALLABY uses SOFIA-X (T. Westmeier et al. 2022), which is a parallelized version of SOFIA-2 (P. Serra et al. 2015; T. Westmeier et al. 2021) designed for the full WALLABY observations.

While WALLABY has detected the H I content of 2419 galaxies in the Pilot Survey phase, not all of these are suitable for the study of asymmetries. N. Deg et al. (2023) noted that measuring 3D asymmetry reliably requires the galaxy be resolved by at least four resolution elements. This requirement matches the 505/2419 detections for which kinematic modeling has been attempted (N. Deg et al. 2022; C. Murugeshan et al. 2024). N. Deg et al. (2022) set the modeling criteria of those galaxies with a SOFIA-2 ell_maj > 2 beams or the integrated $\log_{10}$(S/N) > 1.25. S/N is integrated across the detection (T. Westmeier et al. 2021), and ell_maj is a measure of the size along the major axis that corresponds to ~ half the diameter of kinematically modeled disks (N. Deg et al. 2022). Moreover, since the kinematic models applied assume

Table 1
Summary of the WALLABY Detections for Which 3D Asymmetries Were Measured

Sample	Number
Total WALLABY Detections, Pilot Phase 1 and 2	2419
Kinematic Modeling Attempted	505
Modeling Attempted and $A_{3D} \geqslant 0$	158
Successfully Modeled and $A_{3D} \geqslant 0$	84
Model Failure and $A_{3D} \geqslant 0$	74
Modeling Attempted and $\log(M/M_\odot) \geqslant 9.2$	384
Modeling Attempted, $A_{3D} > 0$, and $\log(M/M_\odot) \geqslant 9.2$	116
Successfully Modeled, $A_{3D} > 0$, and $\log(M/M_\odot) \geqslant 9.2$	67
Model Failure, $A_{3D} > 0$, and $\log(M/M_\odot) \geqslant 9.2$	49

axisymmetry, one might expect the success of the kinematic models to be anticorrelated with the asymmetries.

Most WALLABY detections have ell_maj < 7 beams. Based on the results of N. Deg et al. (2023) and N. Giese et al. (2016), these detections are too poorly resolved for calculations of the spatial (2D) asymmetries, despite them being resolved enough for reliable 3D asymmetries. We therefore calculate both 1D and 3D asymmetries for all WALLABY galaxies where kinematic modeling was attempted. The most important difference between the two is that the background correction of the 1D measures uses the noise in the masked spectra rather than the noise in the cube. Both quantities are calculated using the 3DACS code released in N. Deg et al. (2023).

Using the procedure described above, we recover 1D and 3D asymmetries of the 116/384 (~30%) Pilot Survey detections for which kinematic models were attempted with $\log_{10}(M_{H\,I}/M_\odot) \geqslant 9.2$. The first rows of Table 1 summarize the number of WALLABY detections, the number for which kinematic modeling was attempted, and the set of those with measured asymmetries (i.e., for which $P < B$ in Equation (14)).

For each WALLABY detection, there are a number of properties that are necessary to consider for comparisons to SIMBA. These include the H I mass $M_{H\,I}$, distance D, inclination i, rms noise σ, and size on the sky ell_maj. We take $M_{H\,I}$ and D from N. Deg et al. (2024), σ is directly calculated in 3DACS, and ell_maj is from the WALLABY releases (T. Westmeier et al. 2022; C. Murugeshan et al. 2024). With σ and masks within which the asymmetries are calculated, $\log_{10}$(S/N) can be computed as well. Figure 8 summarizes these properties along with 3D and 1D asymmetries for the full sample of detections where kinematic modeling was attempted as well as the subsamples of kinematically modeled galaxies and those where the modeling failed.

A few things are apparent when examining the histograms in Figure 8. The successfully modeled galaxies and those where the modeling failed have similar distributions of $M_{H\,I}$, D, i, and σ. There is, however, a difference between D for detections where kinematic modeling was attempted and D for detections with measured asymmetries. The larger sample reaches to higher distances, which suggests that those galaxies, which are smaller on the sky, end up have an unmeasurable 3D asymmetry owing to their smaller size. The more interesting difference is that the kinematically modeled subsample does not extend to 3D or 1D asymmetries as high as the ones where
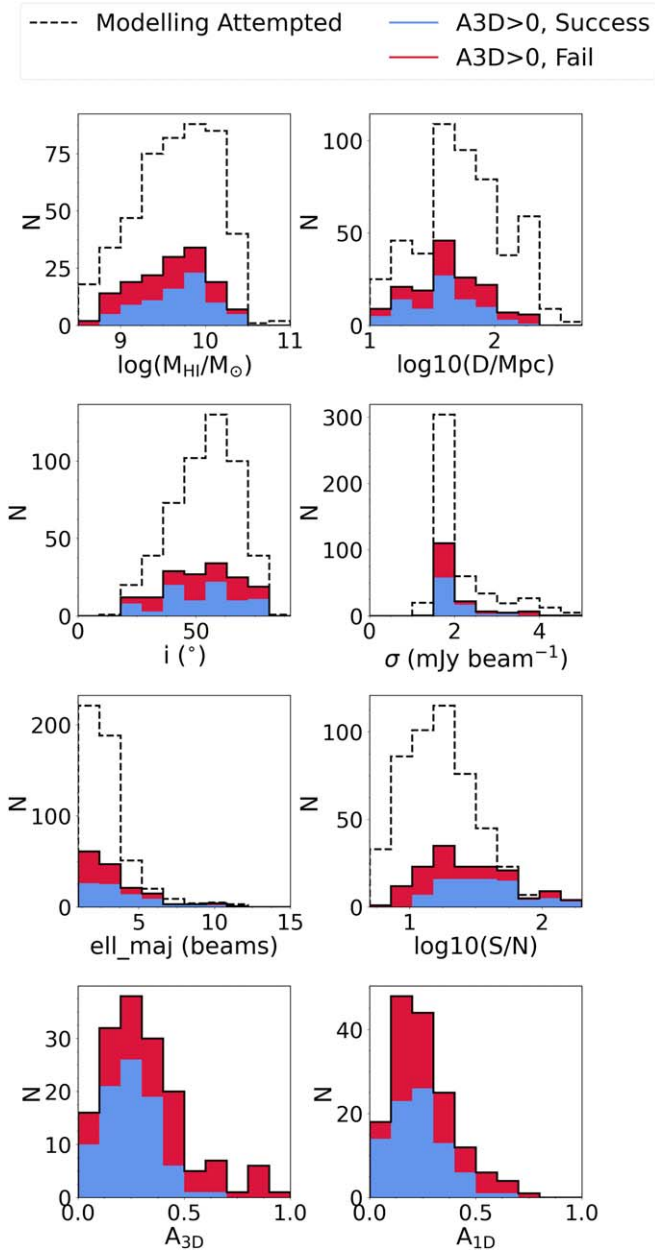
Figure 8. Histograms of the properties of WALLABY detections. The dashed black lines show the full set of detections where kinematic modeling was attempted. The blue shaded regions show those detections where the kinematic modeling was successful and they have measured asymmetries, while the red shaded region shows those where the kinematic modeling failed but they still have measured asymmetries. In the top three rows, the ratio of the red plus blue histograms (the solid black line) to the dashed histogram is equal to the fraction of galaxies for which asymmetries were measured.

Figure 9. Comparison of the 1D and 3D asymmetries of WALLABY detections with $\log_{10}(M_{\rm H\,I}/M_{\odot}) \geqslant 9$. The size of the points correlates to their size on the sky, and the colorbar identifies their S/N. The stars show galaxies where kinematic modeling is successful, while the circles show those without kinematic models. Maps and spectra for the detections labeled A, B, C, D, and E are shown in Figure 10.

the modeling failed. But the existence of unmodeled galaxies with low asymmetries as well as modeled galaxies with high asymmetries indicates that asymmetry alone is not a predictor of the success of the kinematic modeling.

To compare WALLABY to SIMBA, it is necessary for the mock observations to be reliable, which is why we require $\log_{10}(M_{\rm H\,I}/M_{\odot}) \geqslant 9$ among those galaxies (see Section 2.2). To facilitate such a comparison, a mass cut of $\log_{10}(M_{\rm H\,I}/M_{\odot}) \geqslant 9.2$ is applied to the WALLABY sample to produce the desired mass limit when coupled with the matching method discussed in Section 4.2. The number of galaxies in this mass cut subsample is listed in the bottom rows

of Table 1, and Figure 9 shows the relationship between the 3D and 1D asymmetries for this population.

A number of key properties of the WALLABY sample are apparent in Figure 9. First, as suggested by the bottom row of Figure 8, the successfully modeled detections and those where the modeling failed have different asymmetry distributions. The kinematically modeled galaxies tend to have lower asymmetries, and there are very few with "extreme" asymmetries in either 1D or 3D, where $A \geqslant 0.5$. This is a statistical trend, but, as with Figure 8, this plot shows that, on an individual galaxy basis, the specific measured asymmetry does not indicate whether a galaxy is kinematically modelable. At high S/N, the galaxies tend to be larger, which is expected, as S/N correlates with galaxy size (N. Deg et al. 2022; T. Westmeier et al. 2022). More importantly, high-S/N detections tend to have lower A_{1D} but a full range of A_{3D}, in line with the results for the noiseless SIMBA mocks in Section 3.2, further underscoring the power of 3D asymmetries for identifying disturbed systems.

Examples of systems with high A_{1D} and/or A_{3D} are shown in Figure 10 for illustrative purposes. The most common drivers for extreme 3D asymmetries in well-resolved detections are (a) extended tidal features that cause the SOFIA-2 center point to be away from the expected kinematic center like in WALLABY J100903-290239 (row A of Figure 10), and (b) galaxy pairs connected by large tidal bridges as in WALLABY J094919-475749 (row B of Figure 10). In both of these cases, it may be possible to kinematically model the main galaxy or galaxies. In the case of WALLABY J103442-283406 (row C of Figure 10), the detection is an entire interacting group that was examined in detail by T. O'Beirne et al. (2024).

At more moderate resolutions, the extreme asymmetries are more often caused by pairs of galaxies being close enough together that SOFIA-2 identified them as a single source like WALLABY J130810+044441 (row D of Figure 10). There are also detections like WALLABY J165758-624336 (row E of Figure 10) with high A_{1D} but moderate A_{3D}. These tend to be small galaxies with low S/N where the background correction is likely underestimated for the 1D asymmetries, leading to their larger A_{1D}. In rows A–C of Figure 10, A_{1D} is not
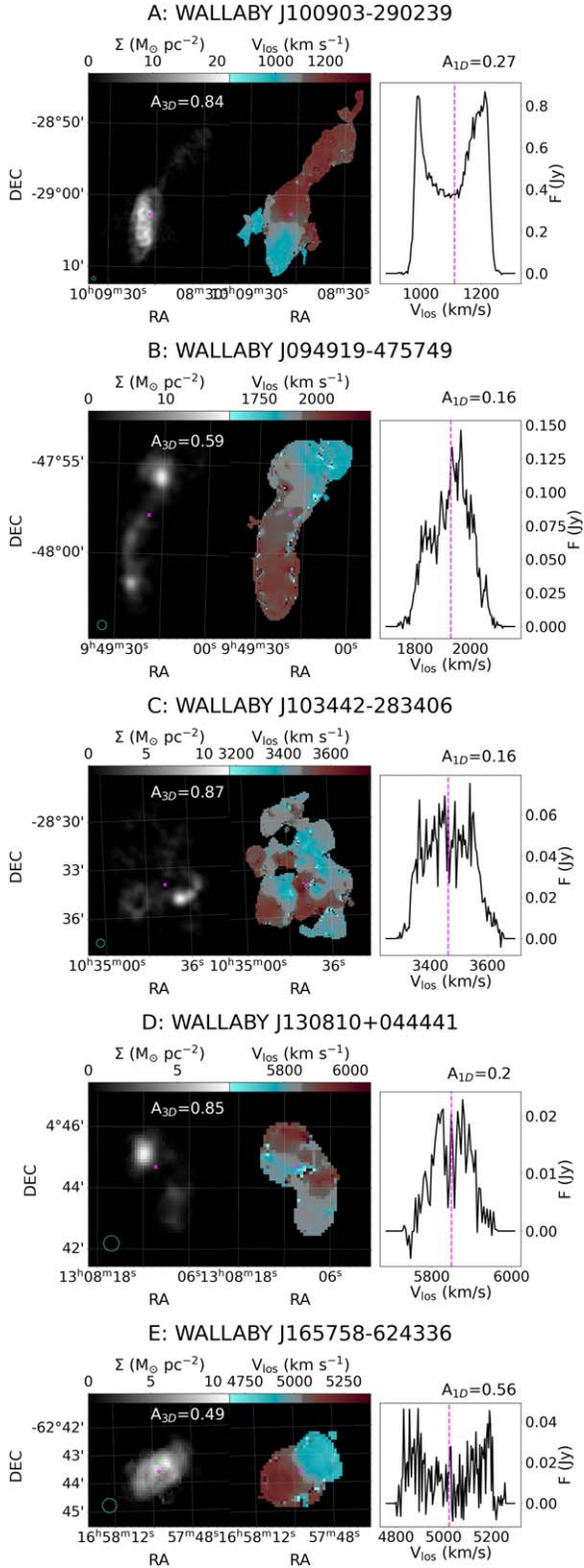
Figure 10. Moment maps and spectra for a set of detections with extreme asymmetries, labeled A–E in Figure 9 to illustrate different drivers of asymmetry. The cyan circles in the lower left of the moment 0 map panels show the size of the beam. The magenta x symbols and vertical lines in the maps and spectral plots show the SOFIA-2 center. This center is used for the calculation of the asymmetries listed in the moment 0 plot (3D) and spectra (1D).

particularly high despite the large disturbances to the detections, highlighting the power of 3D asymmetries at identifying strongly disrupted objects. It appears that, for the most

asymmetric detections (those with $A_{3D} > 0.5$), it is gas that lies beyond the main disk (either in tidal features or other galaxies) that drives the asymmetry. Therefore, selecting detections with $A_{3D} > 0.5$ will reliably find systems with such extended features at the WALLABY resolution and sensitivity.

4.2. SIMBA and WALLABY

To compare SIMBA to WALLABY, it is necessary to generate WALLABY-like SIMBA mocks with similar properties to the WALLABY sample. Our mock SIMBA sample must have masses, distances, inclinations, and noise distributions similar to those seen in Figure 8.

To build our mock sample, we select WALLABY detections on which modeling was attempted and then match each one to a SIMBA galaxy with similar properties. In detail, for each WALLABY detection with H I mass $M_{H\,I,W}$, a SIMBA galaxy with H I mass $M_{H\,I,S}$ in the range $M_{H\,I,S} \in [M_{H\,I,W}10^{-0.2}, M_{H\,I,W}10^{+0.2}]$ is randomly selected from the sample of 789 galaxies that fit the criteria of Section 3.1. A mock H I cube is made of that SIMBA galaxy using our Scanline Tracing MFM method, where the galaxy is placed at the WALLABY detection's recovered distance and inclination. Gaussian noise is then added and convolved by the $30''$ WALLABY beam such that the resulting noisy cube has the same noise rms as the WALLABY detection. Finally, we measure A_{1D} and A_{3D} of the paired SIMBA detection in the same fashion as the WALLABY detection, running SOFIA-2 on the noisy mock and adopting the resulting SOFIA-2 mask and center point in 3DACS.

It is possible to increase the matched sample by creating multiple SIMBA realizations of the WALLABY galaxies. In each realization, one SIMBA galaxy is generated for each WALLABY galaxy. Ultimately, we generate 20 realizations, providing $20\times$ more mock observations than WALLABY detections. While a specific SIMBA galaxy will appear multiple times in the full set of realizations, it will have varying distances, viewing angles, and orientations relative to the observer each time, which produce different measured asymmetries.

As with WALLABY, it is possible for the mock WALLABY observations to have noise such that $P < B$ in Equation (14), and no intrinsic measure of the asymmetry is recovered. As noted in Section 4.1, only 30% of WALLABY detections for which kinematic modeling was attempted have a measured asymmetry. For our mock WALLABY-like SIMBA cubes, the asymmetries are measured for 23% of the mocks. This is slightly lower than the WALLABY fraction, but not inconsistent with it, given the relatively small sample sizes in question.

We quantitatively compare the distribution of measured WALLABY and SIMBA asymmetries using the PQMass test (P. Lemos et al. 2024). The PQMass test performs a Pearson chi-square test by binning our chosen parameter space of (A_{1D}, A_{3D}) using a Voronoi tessellation for a set of points of the SIMBA mock. We elect to use 10 bins. The PQMass test recovers that the probability that SIMBA and WALLABY asymmetry samples are drawn from the same distribution is $p \sim 5.4\% \pm 0.2\%$, where the final value is calculated as an average from ~1000 runs of the test, which vary through different Voronoi binning. The uncertainty is derived from the standard deviation across the runs. While relatively low, a ~5% probability is sufficiently large that we cannot conclude that the SIMBA and WALLABY asymmetry distributions are
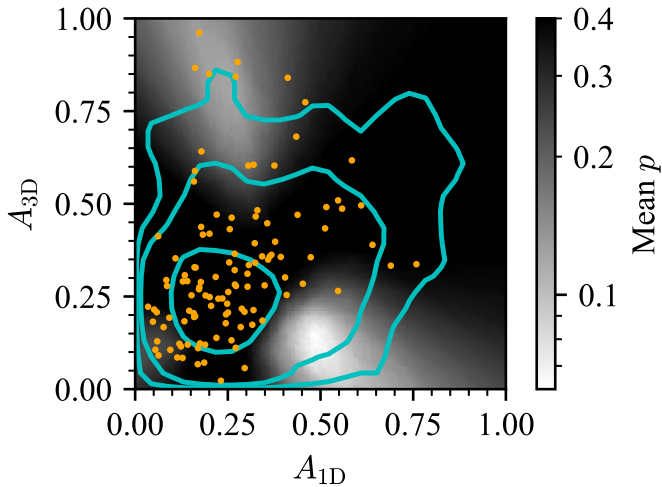
Figure 11. Map of the asymmetry distributions for the WALLABY sample and the WALLABY-like SIMBA mocks. The cyan contours draw the SIMBA distribution for the count-wise 68th, 95th, and 99th percentiles. The orange dots are the individual WALLABY measures. The underlying map shows the mean p-value for binomial tests averaged across different binnings of the A_{1D}–A_{3D} plane.

inconsistent with each other. To make such a conclusion, we will require a significantly larger sample of WALLABY observations as well as simulated galaxies.

Figure 11 overlays the SIMBA asymmetry distribution over the WALLABY detections as contours in order to more closely examine the similarities and differences between the two distributions. The grayscale color map in Figure 11 shows the p-value for the null hypothesis that the asymmetries sample a given bin at the same rate. This p-value should not be taken as a rigorous measure, but rather it is intended to illustrate the discrepancy between the SIMBA and WALLABY samples: it is calculated using the binomial test for the different PQMass Voronoi bins, averaged across multiple binnings.

Figure 11 illustrates that there are two regions in the A_{1D}–A_{3D} where the WALLABY and SIMBA distributions appear to differ, which drive the final PQMass value of ~5%. First, the high-A_{3D}, low-A_{1D} corner shows a significant difference driven by an overdensity of WALLABY detections. These detections, as discussed in Section 4.1 and illustrated in Figure 10, mostly consist of interacting galaxies where the SOFIA-2 center is drawn away from the principal galaxy, increasing the spatial asymmetry. While this same behavior can happen in SIMBA, it occurs for less than 1% of SIMBA mocks as indicated by the 99% contour limit. This hints at a possible difference between WALLABY and SIMBA, but there are other possible causes of this difference, such as environmental selection effects.

The second region where a discrepancy is noticeable is in the moderate-A_{1D}, low-A_{3D} region. This region is overpopulated by the SIMBA mocks compared to WALLABY detections. A possible explanation is that the SIMBA mocks are under-resolved relative to their WALLABY counterparts, which could occur, for example, if the SIMBA disks are smaller than the WALLABY ones at a given M_{HI} (such that the spatial contribution to A_{3D}, and therefore A_{3D} itself, is too low). Overall, however, these differences are small, and we leave a detailed investigation of the causes of these differences to future work.

5. Discussion and Conclusions

We have presented a Scanline Tracing method to create mock H I data cubes for simulated galaxies, reducing the shot noise along the spectral axis of the mock that makes a spurious contribution to asymmetry measures. We apply this technique to generate WALLABY survey–like H I data cubes of simulated galaxies from the SIMBA 50 Mpc simulations, and compare 1D and 3D asymmetries therein. We find hints of an excess of high-asymmetry systems in WALLABY compared to the SIMBA mocks, though that difference is not statistically significant as measured by a PQMass test of the distribution of points in A_{1D} and A_{3D}.

The Scanline Tracing method developed in Section 3.1 can be used to create mock H I cubes for both SPH and MFM hydrodynamical simulations. While this approach introduces additional operations in the computation of the different fields, it avoids the shot noise introduced by the particle-centric method adopted by the default MARTINI settings, as shown in Figures 1 and 2. This advantage is considerable for the study of asymmetry in marginally resolved simulations. However, as the number of particles increases, it is expected that the Particle method will converge to the Scanline Tracing method while offering greater computational ease. For cooler gas (see S. Ploeckinger et al. 2023), the resolution necessary for the particle approach is likely to increase. Currently, for asymmetries in the 50 Mpc SIMBA simulation, the Scanline Tracing method shows noticeable differences with the MARTINI default particle-centric method as seen in Figure 5. Unlike the Particle method, Scanline Tracing will, in the lower resolutions, have the propensity to oversmooth spectra. This error is less evident than the Particle method's shot noise, which may prove more perverse.

In Section 4.1, we measured A_{1D} and A_{3D} asymmetries for the sample of WALLABY pilot detections for which kinematic modeling was attempted. As shown in Figure 9, detections where the kinematic modeling was successful had fewer extreme asymmetries than those where the modeling failed. However, there is a large scatter and the correlation is not statistically significant. Upon inspection (Figure 10), the WALLABY detections with relatively high S/N and $A_{3D} \gtrsim 0.5$ tend to be interacting systems or systems with extended tail-like features. Asymmetry may be an efficient way to detect these systems using H I data alone, which is particularly useful in regions where multiwavelength data are scarce, such as the Zone of Avoidance.

Figure 11 illustrates that our mock WALLABY-like SIMBA samples show signs of discrepancy in their A_{1D} and A_{3D} when compared to WALLABY, even when controlled for mass, distance, and noise. This may hint at potential deviations between the SIMBA galaxy evolution model and the H I distributions in WALLABY detections. Although the PQMass p-value of ~5% indicates that these deviations are not statistically significant on the whole, we can nonetheless speculate on the potential drivers of lower asymmetries in SIMBA galaxies compared to observations. For example, the high-A_{3D}, low-A_{1D} corner where WALLABY detections out-populate the SIMBA mocks may be caused by the overly hot SIMBA IGM (R. Davé et al. 2017; R. J. Wright et al. 2024), which might inhibit structures like H I bridges and tidal features that drive the WALLABY asymmetries. Another possibility is that the WALLABY sample is biased to high asymmetries, perhaps owing to the group and cluster environments

preferentially probed by the Pilot Survey fields (T. Westmeier et al. 2022; C. Murugeshan et al. 2024).

Although our analysis is limited by the relatively low number of H I detections in the WALLABY Pilot Survey detections and the relatively modest particle masses and resolutions in the SIMBA 50 Mpc simulation, the quantitative comparisons between asymmetries in H I detections and in simulations presented in this paper are among the first of their kind—and a prelude of things to come in this space. More thorough comparisons will be enabled with the full statistical power of WALLABY as the complete survey is released. It will also be possible to compare different subgrid physics and dark matter models, both within simulations such as SIMBA as well as across different simulations, in particular as the latter increase in volume and in resolution. This opens new avenues for comparing simulations with observations to determine how various physical phenomena drive H I morphological asymmetries.

ORCID iDs

Nathan Deg https://orcid.org/0000-0003-3523-7633
Kristine Spekkens https://orcid.org/0000-0002-0956-7949
Marcin Glowacki https://orcid.org/0000-0002-5067-8894
Kyle A. Oman https://orcid.org/0000-0001-9857-7788
Marc A. W. Verheijen https://orcid.org/0000-0001-9022-8081
Helga Dénes https://orcid.org/0000-0002-9214-8613
Jonghwan Rhee https://orcid.org/0000-0001-8496-4306
Luca Cortese https://orcid.org/0000-0002-7422-9823
Barbara Catinella https://orcid.org/0000-0002-7625-562X

References

Abruzzo, M. W., Narayanan, D., Davé, R., & Thompson, R. 2018, arXiv:1803.02374
Bilimogga, P. V., Oman, K. A., Verheijen, M. A. W., & van der Hulst, T. 2022, MNRAS, 513, 5310
Blyth, S., Baker, A. J., Holwerda, B., et al. 2016, in MeerKAT Science: On the Pathway to the SKA (Trieste: SISSA), 4
Bok, J., Blyth, S. L., Gilbank, D. G., & Elson, E. C. 2019, MNRAS, 484, 582
Bradski, G. 2000, Dr. Dobb's Journal of Software Tools, 120, 122
Conselice, C. J. 2003, ApJS, 147, 1
Davé, R., Anglés-Alcázar, D., Narayanan, D., et al. 2019, MNRAS, 486, 2827
Davé, R., Rafieferantsoa, M. H., Thompson, R. J., & Hopkins, P. F. 2017, MNRAS, 467, 115
Deg, N., Arora, N., Spekkens, K., et al. 2024, ApJ, 976, 159
Deg, N., Blyth, S.-L., Hank, N., Kruger, S., & Carignan, C. 2020, MNRAS, 495, 1984
Deg, N., Perron-Cormier, M., Spekkens, K., et al. 2023, MNRAS, 523, 4340
Deg, N., & Spekkens, K. 2019, Mock Cube Generator Suite, https://github.com/CIRADA-Tools/MCGSuite
Deg, N., Spekkens, K., Westmeier, T., et al. 2022, PASA, 39, e059
English, J., Richardson, M. L. A., Ferrand, G., & Deg, N. 2024, CosmosCanvas: Useful Color Maps for Different Astrophysical Properties, Astrophysics Source Code Library, ascl:2401.005
Espada, D., Verdes-Montenegro, L., Huchtmeier, W. K., et al. 2011, A&A, 532, A117
Gensior, J., Feldmann, R., Reina-Campos, M., et al. 2024, MNRAS, 531, 1158
Giese, N., vanderHulst, T., Serra, P., & Oosterloo, T. 2016, MNRAS, 461, 1656
Gingold, R. A., & Monaghan, J. J. 1977, MNRAS, 181, 375
Glowacki, M., Deg, N., Blyth, S.-L., et al. 2022, MNRAS, 517, 1282
Glowacki, M., Elson, E., & Davé, R. 2020, MNRAS, 498, 3687
Hambleton, K. M., Gibson, B. K., Brook, C. B., et al. 2011, MNRAS, 418, 801
Haynes, M. P., Hogg, D. E., Maddalena, R. J., Roberts, M. S., & van Zee, L. 1998, AJ, 115, 62
Holwerda, B. W., Bigiel, F., Bosma, A., et al. 2023, MNRAS, 521, 1502
Holwerda, B. W., Pirzkal, N., de Blok, W. J. G., et al. 2011, MNRAS, 416, 2401
Hopkins, P. F. 2015, MNRAS, 450, 53
Hotan, A. W., Bunton, J. D., Chippendale, A. P., et al. 2021, PASA, 38, e009
Koribalski, B. S., Staveley-Smith, L., Westmeier, T., et al. 2020, Ap&SS, 365, 118
Lelli, F., Verheijen, M., & Fraternali, F. 2014, MNRAS, 445, 1694
Lemos, P., Sharief, S., Malkin, N., Perreault-Levasseur, L., & Hezaveh, Y. 2024, arXiv:2402.04355
Lotz, J. M., Jonsson, P., Cox, T. J., & Primack, J. R. 2008, MNRAS, 391, 1137
Lotz, J. M., Jonsson, P., Cox, T. J., & Primack, J. R. 2010, MNRAS, 404, 590
Lucy, L. B. 1977, ApJ, 82, 1013
Murugeshan, C., Deg, N., Westmeier, T., et al. 2024, PASA, 41, e088
Nelson, D., Springel, V., Pillepich, A., et al. 2019, ComAC, 6, 2
O'Beirne, T., Staveley-Smith, L., Wong, O. I., et al. 2024, MNRAS, 528, 4010
Oman, K. A. 2019, MARTINI: Mock Spatially Resolved Spectral Line Observations of Simulated Galaxies, Astrophysics Source Code Library, ascl:1911.005

Oman, K. A. 2024, JOSS, 9, 6860

Oman, K. A., Marasco, A., Navarro, J. F., et al. 2019, MNRAS, 482, 821

Ploeckinger, S., Nobels, F. S. J., Schaller, M., & Schaye, J. 2023, MNRAS, 528, 2930

Punzo, D., vanderHulst, J., Roerdink, J., Fillion-Robin, J., & Yu, L. 2017, A&C, 19, 45

Reynolds, T. N., Westmeier, T., Staveley-Smith, L., Chauhan, G., & Lagos, C. D. P. 2020, MNRAS, 493, 5089

Rhee, J., Meyer, M., Popping, A., et al. 2023, MNRAS, 518, 4646

Rix, H.-W., & Zaritsky, D. 1995, ApJ, 447, 82

Sancisi, R., Fraternali, F., Oosterloo, T., & van der Hulst, T. 2008, A&ARv, 15, 189

Sazonova, E., Morgan, C., Balogh, M., et al. 2024, OJAp, 7, 77

Serra, P., Westmeier, T., Giese, N., et al. 2015, MNRAS, 448, 1922

Smith, B. D., Bryan, G. L., Glover, S. C. O., et al. 2016, MNRAS, 466, 2217

Thorp, M. D., Bluck, A. F. L., Ellison, S. L., et al. 2021, MNRAS, 507, 886

Wang, J., Koribalski, B. S., Serra, P., et al. 2016, MNRAS, 460, 2143

Watts, A. B., Cortese, L., Catinella, B., et al. 2023, MNRAS, 519, 1452

Watts, A. B., Power, C., Catinella, B., Cortese, L., & Stevens, A. R. H. 2020, MNRAS, 499, 5205

Westmeier, T., Deg, N., Spekkens, K., et al. 2022, PASA, 39, e058

Westmeier, T., Kitaeff, S., Pallot, D., et al. 2021, MNRAS, 506, 3962

Wilkinson, S., Ellison, S. L., Bottrell, C., et al. 2024, MNRAS, 528, 5558

Wright, R. J., Somerville, R. S., Lagos, C. d. P., et al. 2024, MNRAS, 532, 3417

Zaritsky, D., & Rix, H.-W. 1997, ApJ, 477, 118